JOURNAL OF SOLID STATE CHEMISTRY 114, 24–35 (1995)

Crystal and Magnetic Structure of $YBaCuFeO_5$

V. Caignaert, I. Mirebeau,* F. Bourée,* N. Nguyen, A. Ducouret, J-M. Greneche,† and B. Raveau

*Laboratoire CRISMAT–ISMRA, Bd Maréchal Juin, 14050 Caen Cedex, France; *Laboratoire Léon Brillouin (CEA–CNRS), CE-Saclay, 91191 Gif-sur-Yvette Cedex, France; and †Laboratoire de physique des matériaux, Université du Maine, 72017 Le Mans Cedex, France*

Received October 12, 1993; in revised form March 3, 1994; accepted March 3, 1994

The perovskite-like antiferromagnetic compound $YBaCuFeO_5$ was studied by powder neutron diffraction, magnetic susceptibility measurements, and Mössbauer spectroscopy. Crystal structure is analysed in the centrosymmetric space group *P4/mmm* and compared to previous results in the noncentrosymmetric space group *P4mm*. Fe/Cu atoms occupy randomly the oxygen pyramids with iron displaced inside the pyramid with respect to the copper position. The magnitude and the distribution of the quadrupolar splitting obtained by electric field gradient calculations, taking into account the cationic disorder, are in qualitative agreement with those observed by Mössbauer spectroscopy in the paramagnetic range. Magnetic susceptibility and neutron powder diffraction reveal two magnetic transitions at $T_{N1} = 441(2)$ K and $T_{N2} \approx 230$ K. Between T_{N1} and T_{N2}, the magnetic structure is based on a unit cell related to that of the nuclear structure by $a_{mag} = \sqrt{2}a_{nuc}$ and $c_{mag} = 2c_{nuc}$. The magnetic moments are coupled antiferromagnetically within each $[CuFeO_5]_\infty$ layer with the stacking sequence along c: $+--+$. The magnetic structure is refined with moments tilted with respect to the c axis. The large reduction of magnetic moment observed by neutron powder diffraction is explained by the cationic disorder. Below T_{N2} the magnetic structure is incommensurate with a short-range order.

1. INTRODUCTION

The substitution of iron for copper in layered cuprates has been extensively studied by different methods—neutron diffraction, Mössbauer spectroscopy, and magnetic measurements—in order to understand the relationship between superconductivity and magnetism in these materials. Iron can indeed be used as a probe, especially when it replaces copper in pyramidal sites, leading to a dramatic decrease of the superconducting properties. Nevertheless, the numerous Mössbauer studies performed on iron-doped cuprates do not allow us to determine the exact position of iron in the FeO_5 pyramid when it is substituted for copper so that assumptions have to be made for the interpretation of the spectra. In this respect, the structure of $YBaCuFeO_5$ is of interest since it is built up of only $(Cu, Fe)O_5$ pyramids. The structure was first solved from powder neutron diffraction data in the space group *P4mm* (1) and confirmed from X-ray diffraction single-crystal data (2). In fact, a more symmetric group *P4/mmm* was also possible, but the authors of (1) clearly indicate that the space group *P4mm* was chosen as the most symmetrical allowing two different sites for iron and copper ions: the reason for this choice is the presence of two components, in the Mössbauer spectrum registered at room temperature, attributed to iron in two crystallographic sites. However, further studies (3–6) have concluded that Mössbauer spectra of $YBaCuFeO_5$ and $LnBaCuFeO_5$ display only one component with a broad distribution of hyperfine field. Based on the assertion that there exist two distinct crystallographic sites in the structure of $YBaCuFeO_5$, Meyer *et al.* (3) and Pissas *et al.* (4–6) concluded that iron is located only on one type of site exclusively, called $1b_1$, whereas copper is located on the other site, called $1b_2$. Now, as mentioned above, the existence of two crystallographic sites was postulated in order to explain the two components in the Mössbauer spectrum. This suggests that the space group *P4mm*, which was chosen first from Mössbauer data, may be questionable in spite of the very good results obtained from the neutron diffraction refinements. Moreover, the asymmetric broadening of the lines of the magnetic Mössbauer sextet is, according to us, not really compatible with an ordered distribution of iron and copper on two distinct sites. We report here on the re-examination of the nuclear structure of this phase and on its magnetic structure and Mössbauer study performed on the same sample and supplemented by electric field gradient (EFG) calculations in a point charge model.

2. EXPERIMENTAL DETAILS

Synthesis. Stoichiometric amounts of Y_2O_3, $BaCO_3$, CuO, and Fe_2O_3 were thoroughly mixed and fired at 950°C in air. The powder was ground and heated again at 1000°C over several days. In order to avoid a possible small excess of oxygen, the sample was finally annealed at 500°C under argon for 5 hr and then slowly cooled. Samples quenched in air or annealed under oxygen were also synthesised in order to compare their magnetic properties.

0022-4596/95 $6.00

Powder diffraction. The powder X-ray diffraction pattern was registered with a Seifert C3000 diffractometer using a primary monochromator selecting $CuK\alpha_1$ radiation. It was indexed in the perovskite-related tetragonal cell with $a \approx a_p$ and $c \approx 2a_p$. No trace of impurity was detected by X-ray diffraction. Neutron powder diffraction (NPD) data were collected on the 3T2 diffractometer at LLB Saclay, using a neutron wavelength of 1.2268 Å and a 2θ step scan of 0.05°. Data were registered over the Q range $0.4 < Q < 9$ Å^{-1} at room temperature. In order to study the magnetic structure, NPD data were also collected between 8 and 450 K on the G6-1 spectrometer at LLB Saclay using a wavelength of 4.733 Å. Due to this long wavelength, the Q domain was limited to $Q < 2.5$ Å^{-1}. The nuclear and magnetic structure refinements were performed using the profile-fitting program "FULLPROF" (7).

Magnetic measurements. The magnetic susceptibility was measured with the Faraday method using a Cahn RG microbalance, between 77 and 800 K, with an applied field of 3000 G.

Mössbauer spectroscopy. The Mössbauer resonance spectra were obtained in a transmission geometry with a constant acceleration spectrometer using a ^{57}Co source diffused into a rhodium matrix and held at room temperature. The powder sample, which contained 10 mg of natural iron per cm^2, was studied at 4.2, 293, and 530 K. The isomer shift values are given with respect to metallic iron at room temperature.

3. NUCLEAR STRUCTURE

The neutron powder diffraction data were analysed first with a "whole pattern fitting" algorithm in order to determine accurately the profile shape function, background, and cell parameters. This preliminary analysis has the advantage of providing a good estimate of the R_{wp} and χ^2 that could be reached during the structure refinement. Moreover, the result of this refinement does not depend on the choice of the space group *P4/mmm* or *P4mm*. This whole pattern fitting (including the magnetic peaks) led to $R_{wp} = 4.6\%$ and $\chi^2 = 2.2$. No significant anisotropic broadening of the peaks appeared so that the sample could be considered free of strain or particle size effect. Otherwise, two small residual peaks remained which cannot be indexed in the $YBaCuFeO_5$ cell. These peaks have been attributed to a small impurity which will be observed by Mössbauer spectroscopy (see Section 5).

The Rietveld refinement was initiated in the *P4/mmm* centrosymmetric space group. The fitting of the two atomic positions ($z_{Cu,Fe}$ and z_{O2}) and the five thermal parameters led to $R_{wp} = 7.22\%$ and $\chi^2 = 5.19$. After the refinement of anisotropic thermal parameters for the Ba site and the O_1 site ($\frac{1}{2}$, $\frac{1}{2}$, 0) the R_{wp} and χ^2 were lowered to 6.79% and 4.60. In spite of a good value of R_i (=5.45%), a careful observation of the difference profile showed a systematic discrepancy between the observed and calculated intensities: the even h, k, 0 peaks were observed to be more intense than the calculated ones, while the h, k, l peaks with h, $k = 2n + 1$ and $l = 4n$ were too weak. At this stage of the refinement, a Fourier-difference synthesis was made which revealed a significant anisotropic residual on both sides of the Cu/Fe position along the **c** axis (Fig. 1). This suggested a splitting of the Cu/Fe position: the more intense residual, inside the pyramid, was attributed to iron ($z \approx 0.25$) and the less intense, near the basal plane of the pyramid, to copper ($z \approx 0.28$). The refinement with two half-occupied sites converged to $R_{wp} = 5.59\%$ and $\chi^2 = 3.11$. Fitting the magnetic peaks as a second phase led to an even better agreement: $R_{wp} = 5.43\%$ and $\chi^2 = 2.94$. The refined values of the structural parameters are listed in Table 1 and the final observed and calculated diffraction profiles are drawn in Fig. 2.

Though this solution, involving the space group *P4/mmm*, was very satisfying, it was necessary to compare it to that obtained with the space group *P4mm*, especially since the Fourier difference is sensitive to the used space group. Seven sites were necessary in the second model and all the z atomic coordinates were adjustable parameters. One of them (Y site) was fixed in order to avoid a global shift of the structure along z during the refinement. The previous published positional parameters (1, 2) were used to initiate the refinement. When the thermal factors of iron and copper sites were forced to be equal, the R_{wp} and χ^2 were 6.8% and 4.6. If they were free, the refinement was slightly oscillating and gave a small value for the copper thermal factor and a high value (≈1 Å^{-2}) for the iron thermal factor. Moreover, the difference profile, although reduced, always showed the same residual as mentioned above. The refined structural parameters, corresponding to this second model with the space group *P4mm*, are given in Table 2. They correspond to significantly higher reliability factors: $\chi^2 = 4.42$, $R_{wp} = 6.66\%$, and $R_N = 5.80\%$.

Clearly the model with space group *P4/mmm* is better than the one with the space group *P4mm* in spite of the larger number of refinable parameters of the latter. The higher χ^2 obtained with the space group *P4mm* is explained by comparing the atomic positions in the two models: in the space groups *P4/mmm* and *P4mm* (Fig. 3), the positions of the oxygen atoms, as well as those of the yttrium and barium sites, are nearly identical. Therefore, with some limited shifts, the oxygen sites, the yttrium site, and the barium site could be described in space group *P4/mmm* instead of *P4mm*. Thus the main difference between the two models is due to the location of transition metal inside the oxygen pyramids: in the *P4mm* space group, each pyramidal layer contains only one posi-

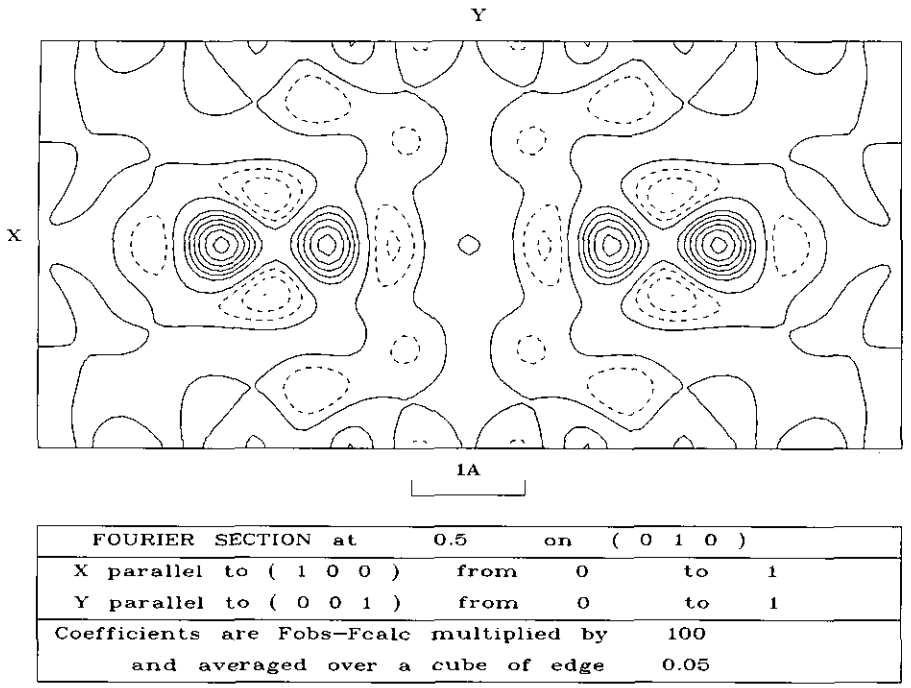

FIG. 1. Fourier-difference section of $YBaCuFeO_5$ at $y = 0.5$. Data were refined using *P4/mmm* space group with copper and iron on the same site (see text).

tion for the transition metal, while two positions are statistically allowed in the first model. The anomalous value of iron and copper thermal parameters, observed in the *P4mm* refinement, shows that each sheet of transition metal has the same mean scattering length.

4. MAGNETIC STRUCTURE

4.1. General Characteristics of the Magnetic Behavior

The inverse molar magnetic susceptibility of $YBaCuFeO_5$ is plotted in Fig. 4. The linear part of the $1/\chi$ versus temperature, fitted with a Curie–Weiss law $\chi = \chi_0 + C/(T - \theta_p)$, leads to a large value of the paramagnetic temperature θ_p: the least-square extrapolation, with the data above 500 K, indeed gives $\theta_p = -810(10)$ K, typical of an antiferromagnetic behavior. A first antiferromagnetic transition is observed at $T_{N1} = 440$ K. Below T_{N1}, the temperature behavior of the $1/\chi$ curve is anomalous. After a maximum at about 330 K, the $1/\chi$ decreases with temperature and a second broad minimum is observed at $T \approx 200$–230 K. This second transition, labelled T_{N2}, is also observed in all the samples whatever the

TABLE 1
Refined Structural Parameters of $YBaCuFeO_5$ at Room Temperature

Atom	Site	x	y	z	B(Å^2) or $\beta_{ij} \times 10^4$	Occupancy
Y	1*b*	0	0	$\frac{1}{2}$	0.43(2)	1
Ba	1*a*	0	0	0	$\beta_{11} = 63(8)$ $\beta_{33} = 112(8)$	1
Cu	2*h*	$\frac{1}{2}$	$\frac{1}{2}$	0.2854(3)	0.22(9)	$\frac{1}{2}$
Fe	2*h*	$\frac{1}{2}$	$\frac{1}{2}$	0.2525(3)	0.27(7)	$\frac{1}{2}$
O1	1*c*	$\frac{1}{2}$	$\frac{1}{2}$	0	$\beta_{11} = 112(8)$ $\beta_{33} = 80(2)$	1
O2	4*i*	$\frac{1}{2}$	0	0.3156(1)	0.57(1)	1

Note. Nuclear cell: $a = 3.8751(1)$ Å, $c = 7.6790(2)$ Å. Space group: *P4*/mmm. Magnetic cell: $a = 5.4799(1)$ Å, $c = 15.3581(3)$ Å. Magnetic moment: $\mu_x = 2.65(13)\mu_B$, $\mu_y = 1.48(15)\mu_B$, $|\mu| = 3.03(5)\mu_B$. $R_p = 4.54\%$, $R_{wp} = 5.43\%$, $R_e = 3.17\%$, $\chi^2 = 2.94$, $R_N = 3.28\%$, $R_M = 14\%$.

TABLE 2
Refined Structural Parameters of $YBaCuFeO_5$ at Room Temperature

Atom	Site	x	y	z (This work)	$(1)^{a,b}$	$(2)^b$	B(Å^2) (This work)
Y	1*a*	0	0	$\frac{1}{2}$	$\frac{1}{2}$	$\frac{1}{2}$	0.47(3)
Ba	1*a*	0	0	0.0118(14)	0.0114(22)	0.0090(8)	0.42(6)
Cu	1*b*	$\frac{1}{2}$	$\frac{1}{2}$	0.7312(10)	0.7275(5)	0.7247(7)	0.05(10)
Fe	1*b*	$\frac{1}{2}$	$\frac{1}{2}$	0.2663(10)	0.2626(6)	0.263(1)	1.04(11)
O1	1*b*	$\frac{1}{2}$	$\frac{1}{2}$	−0.0069(16)	0.0037(23)	−0.001(5)	0.97(5)
O2	2*c*	$\frac{1}{2}$	0	0.3079(11)	0.3219(9)	0.310(2)	0.70(10)
O3	2*c*	$\frac{1}{2}$	0	0.6766(11)	0.6916(9)	0.678(3)	0.52(10)

Note. Space group: *P4mm*.
[a] at 500 K.
[b] The values have been shifted in order to have Y at $z = 0.5$.

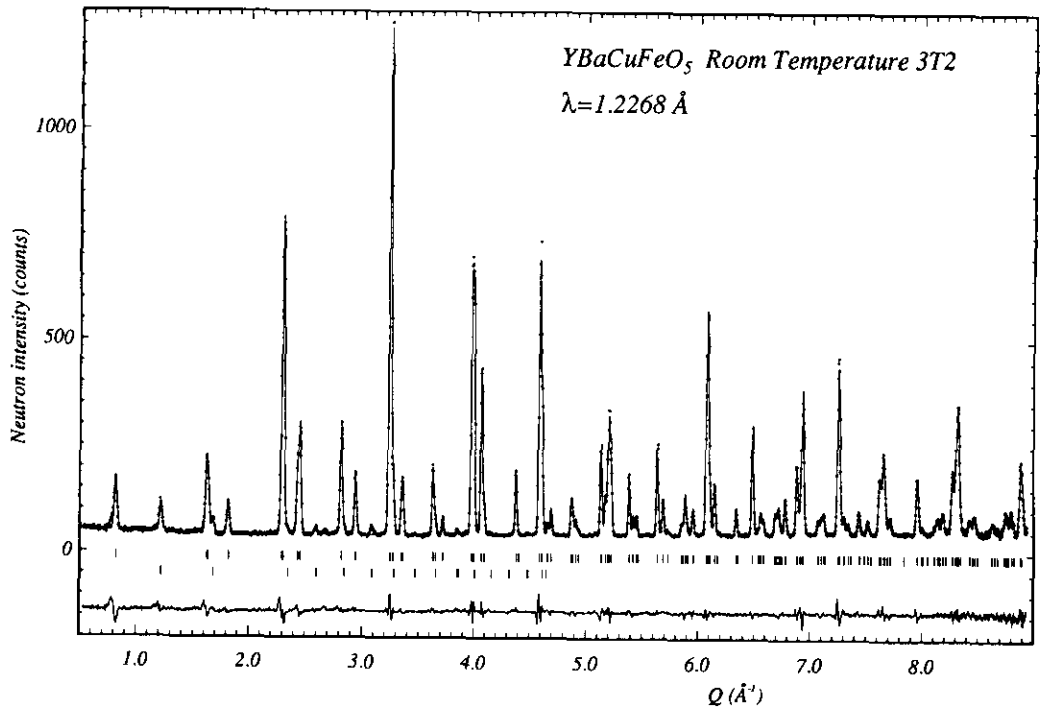

FIG. 2. Final profile fit of $YBaCuFeO_5$ ($P4/mmm$) at room temperature. Ticks below the profile mark the positions of allowed nuclear (top) and magnetic (bottom) reflections. The difference curve is plotted beneath at the same scale.

thermal treatments (see Experimental Details). The mean hyperfine field of iron, obtained by Mössbauer spectroscopy on $YBaCuFeO_5$ (see Fig. 2 in Ref. (3)], was not affected by this transition. However, a plot of the hyperfine field dispersion width factor versus temperature (from Ref. (3)) shows that the decrease of this parameter was more pronounced under 200 K (Fig. 5). One can suggest that this second magnetic transition affects at least the distribution of hyperfine field on iron. The neutron diffraction data clearly reveal these two magnetic transitions (Fig. 6). Between T_{N1} and T_{N2}, the patterns show additional reflections whose nature is purely magnetic. These peaks could be indexed in a magnetic cell related to the nuclear cell with $a_{mag} = \sqrt{2}a_{nuc}$ and $c_{mag} = 2c_{nuc}$. From the temperature dependence of the first magnetic reflection it is possible to estimate the Néel temperature at $T_{N1} = 441(2)$ K, in good agreement with the magnetic susceptibility and Mössbauer measurements (3). Below T_{N2}, the intensity of the magnetic reflections decreases with the temperature, while reflections with a lorentzian

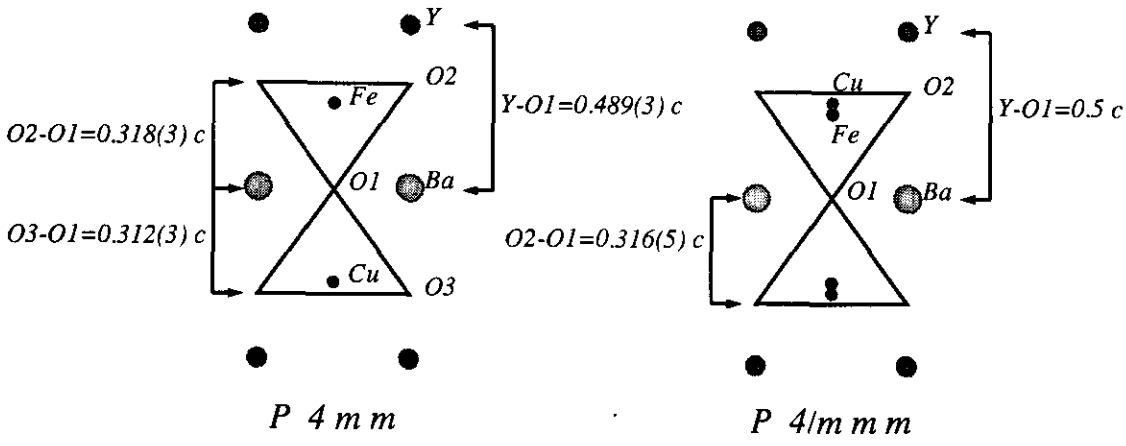

FIG. 3. Schematic drawing of the difference between $P4mm$ and $P4/mmm$ structural models.

shape grow up on each side of the magnetic peaks. These additional reflections were indexed, with respect to the magnetic cell, in an incommensurate cell with a propagation vector (0, 0, 0.212(3)) at $T = 20$ K. The lorentzian shape of these satellites is indicative of a finite antiferromagnetic spin correlation over a short distance. An estimation of the spin correlation length ξ is achieved by fitting the magnetic satellites to a lorentzian shape convoluted with the gaussian resolution function which is given by the simultaneous fit of the commensurate magnetic peak (see inset in Fig. 8). This length does not sensibly change with temperature and is estimated to about 80 Å ($K = 1/\xi = 1.28(1) \times 10^{-2}$). The spin correlation length is slightly larger than the periodicity of the incommensurate magnetic modulation ($\lambda \approx 72$ Å). The sum of the magnetic bragg intensity $I(\frac{1}{2}, \frac{1}{2}, \frac{1}{2})$ and its satellites $I(\frac{1}{2}, \frac{1}{2}, \frac{1}{2})^{\pm}$ increases from T_{N2} to 4 K. It seems also that the increase of the magnetic scattering intensity is more pronounced below T_{N2} (Fig. 7a). In addition to the satellite peaks, below 230 K, a very small peak indexed as $(\frac{1}{2}, \frac{1}{2}, 1)$ in the nuclear cell increases with decreasing temperature: the intensity of this peak is about 4.5% of the $(\frac{1}{2}, \frac{1}{2}, \frac{1}{2})$ magnetic reflection.

4.2. *Rietveld Refinement of the Magnetic Structure*

In order to study the commensurate magnetic structure (between T_{N1} and T_{N2}), we used simultaneously the neutron diffraction data registered on G6-1 and 3T2 at room temperature: three well-individualised magnetic reflections were observed with the first set of data, whereas about 17 reflections were used with the second set of data. In the case of collinear spin models, the magnetic structure profile refinements were performed with the uniaxial configuration spin symmetry (8). As the refinement was found to be rather insensitive to the exact shape of the form factor, the magnetic form factor of Fe^{3+} was used. At room temperature, the only superlattice peaks found correspond to $h/2$, $k/2$, and $l/2$, with h, k, and l odds. The fact that h and k were odds implied that first nearest neighbour Fe (or Cu) atoms within a layer have antiparallel spins. As l was always odd, two atoms separated by **c** have antiparallel magnetic moments. Two collinear models could be derived from these observations: the magnetic moments in the antiferromagnetic layers must be coupled, along the **c** axis, either with the sequence $+[+-]-$ or with the sequence $+[--]+$, where the bracket corresponds to the position of the yttrium. The refinements performed with the magnetic moment directed along the **c** axis gave poor agreement for the two sequences of moments. A better result was obtained assuming magnetic moment lying in the (**a**, **b**) plane ($R_M = 19\%$ on 3T2 data). Nevertheless, it was not possible to conclude between the two stacking sequences of spin

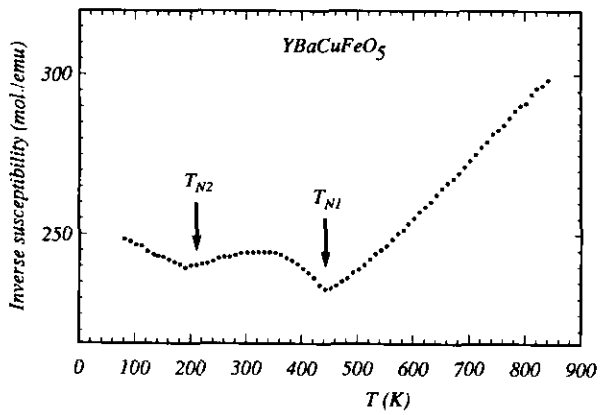

FIG. 4. Plot of the reciprocal molar magnetic susceptibility versus temperature.

ordering along the **c** axis: in fact, since iron possesses the largest magnetic moment and is close to the position $z = \frac{1}{4}$, the two models lead to nearly identical magnetic structure factors and so are indistinguishable. It is worth mentioning that a noncollinear model, with magnetic moments of successive layers rotated by 90° in the (**a**, **b**) plane, will also give the same scattering intensities for powder data.

The results of Mössbauer spectroscopy observations ((3) and this work) suggest that the iron moments at 4 K are not oriented along the crystallographic axes. The tilt of iron moment is probably related to the existence of the incommensurate transition, but may perhaps exist in the commensurate magnetic structure. At room temperature,

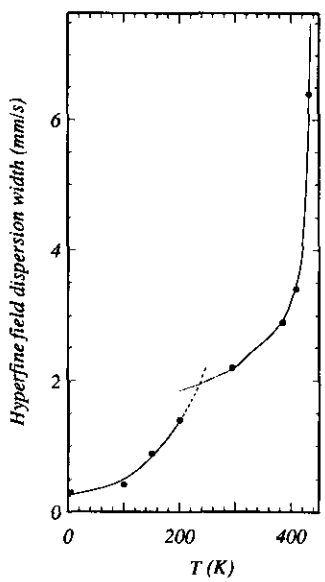

FIG. 5. Plot of the hyperfine field dispersion width factor versus temperature. The data are taken from Ref. (2). The lines are used as a guide for the eyes.

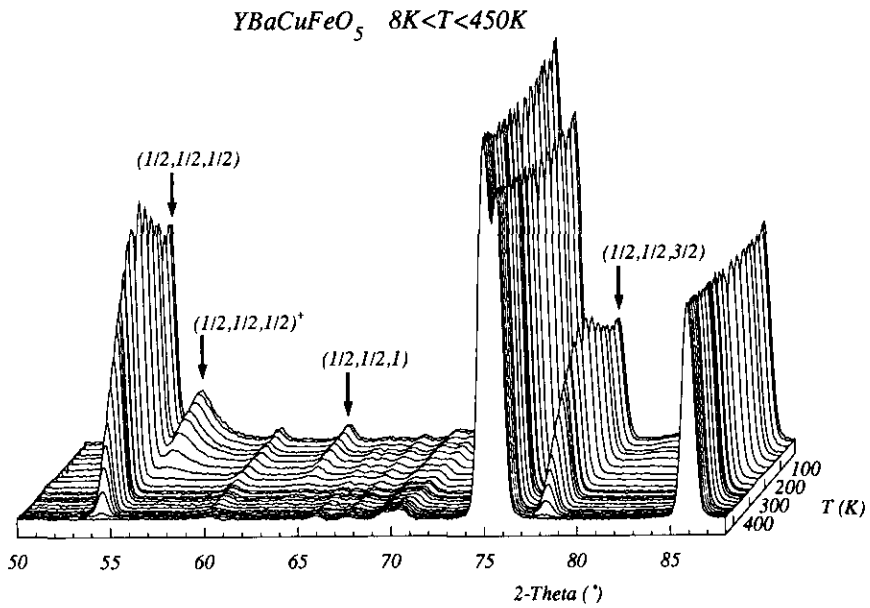

FIG. 6. Part of the neutron diffraction patterns as a function of the temperature.

i.e., for the commensurate magnetic phase, the refinement of the magnetic moments with one component along the **c** axis and the other in the (**a**, **b**) plane, both with the sequence $+[+-]-$, led to a still better result (R_M = 14% on 3T2 data) than the in-plane models. The other models with tilted moments, based on the combination of the two stacking sequences and the "rotating" sequence, were again indistinguishable from each other, due to the nearly special position of iron in the cell. Although the present study shows that the best magnetic structure refinement requires a tilting of the moments with respect to the **c** axis, this result should be confirmed by further investigations with better statistic and resolution at high Q. Figures 3 and 8 show the diffraction profiles at room temperature refined with 3T2 and G6-1 data.

The refinements of magnetic structure, between 200 and 450 K, were performed with the bilayer $(Cu,Fe)O_2$–BaO–$(Cu,Fe)O_2$ antiferromagnetically coupled, i.e., with the sequence $+[+-]-$. The angle between the magnetic moment and the **c** axis is equal to 61 (±2)° and is nearly temperature independent. This value can be compared to that obtained by Mössbauer spectroscopy

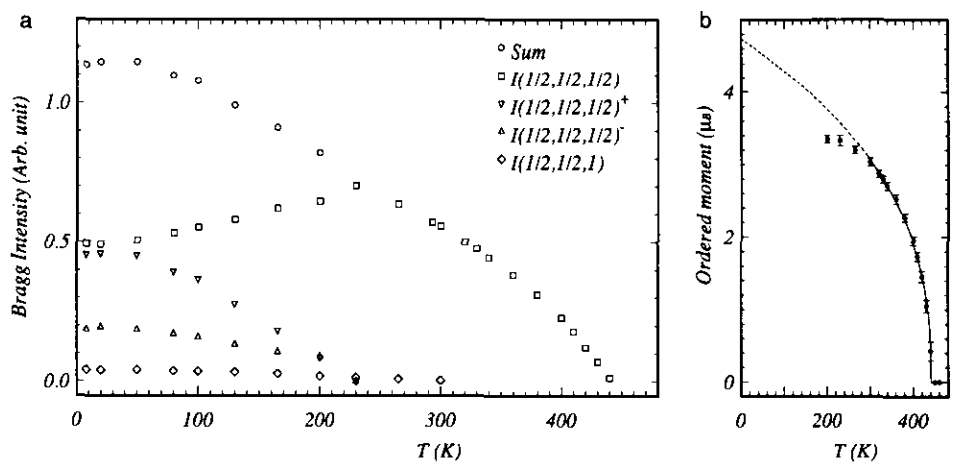

FIG. 7. (a) Intensity of magnetic reflections $I(\frac{1}{2}, \frac{1}{2}, \frac{1}{2})$, $I(\frac{1}{2}, \frac{1}{2}, \frac{1}{2})^{\pm}$ and their sum versus temperature. (b) Value of the total magnetic moment in $YBaCuFeO_5$ versus temperature. The solid line is a fit with a power law $\mu(T) \propto (T_N - T)^{\beta}$, where β is found equal to 0.380(9).

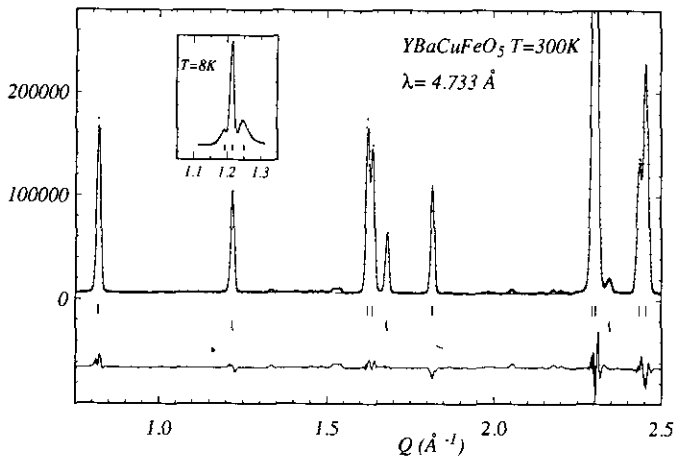

FIG. 8. Final profile fit of the $YBaCuFeO_5$ magnetic structure ($P4/mmm$) at room temperature. Ticks below the profile mark the positions of allowed nuclear (top) and magnetic (bottom) reflections. The inset shows the profile refinement of the magnetic Bragg peak ($\frac{1}{2}$, $\frac{1}{2}$, $\frac{1}{2}$) and its incommensurate satellites at T = 8 K.

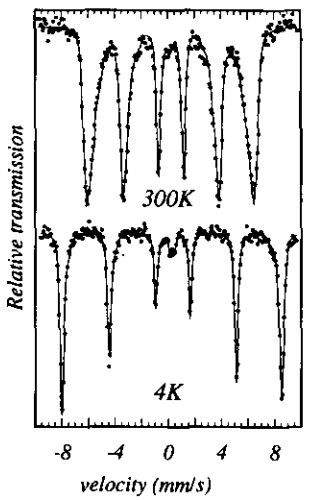

FIG. 9. Mössbauer spectra of $YBaCuFeO_5$ at room temperature and 4.2 K.

(3), i.e., 68° when the quadrupole splitting (QS) value is positive. Figure 7b gives the value of the refined magnetic moment for one copper plus one iron versus temperature. It appears that the extrapolated value of the total moment at low temperature is far from the expected value ($5\mu_B$ + $1\mu_B$) even if we take a probable reduction of moments, due to covalency effects, into consideration. The fit of the magnetic moment with a power law $\mu(T)\,\alpha\,(T_N - T)^\beta$, in the range $0.7 < T/T_N < 1$, gives a critical exponent β = 0.380(9), which rules out the invocation to a spin reduction by 2-D magnetic ordering.

5. MÖSSBAUER STUDY

The Mössbauer spectra, recorded at 4.2 and 300 K, are reported in Fig. 9; they consist of a sextet with well-defined lines at low temperature and a very small paramagnetic contribution in the zero-velocity range (singulet or doublet whose relative intensity is <4%). The asymmetric broadening of the sextet lines has been previously discussed by Meyer *et al.* (3). From our point of view, this asymmetry could be attributed to the cationic surrounding the iron probe as suggested by our EFG calculations (see below). Mössbauer experiments on our sample are in progress, in order to follow the temperature dependence of the hyperfine field. In the present study, we reproduce the spectra by using a fitting procedure which involves a discrete distribution of static hyperfine fields (Table 3 and Fig. 10). The maximum of the distribution is obtained for the hyperfine field values of 51 and 39 T at 4.2 K and room temperature, respectively. These results are in agreement with those observed by Meyer *et al.* (3). The Mössbauer spectrum recorded at T = 530 K (as is shown in Fig. 11) exhibits a slightly asymmetric doublet with broadening wings. A first attempt of fitting was done by introducing two independent paramagnetic components. The site with 8% intensity could be attributed to the residual impurity observed by neutron diffraction. Furthermore, one can also suggest a procedure involving distributions to take into account the different possible local environments of the iron site: it consists in a discrete distribution of quadrupole splitting (P(QS)) linearly correlated with that of the isomer shifts, so as to reproduce the asymmetry. As is shown in Fig. 12, $P|QS|$ exhibits a narrow peak centered around $|QS| \approx 0.2$ mm/sec corresponding to the main component previously observed, and a large tail in the range 0.5–1.6 mm/sec. Assuming that the crystalline structure is not temperature dependent, the quadrupole

TABLE 3
Mössbauer Parameters Derived from the Fitted Spectra

T (K)	δ (mm/sec)	Γ (mm/sec)	2ε (mm/sec)	H_{max} (T)	%
4.2	0.41	0.24	−0.06	51	96
	0.35	0.26	0.30	—	4
293	0.31	0.26	−0.03	39	98
	0.19	0.44	0	—	2
			QS (mm/sec)		
530	0.16	0.31	0.21	—	92
	0.19[a]	0.35	1.13	—	8

Note. δ, Isomer shift referred to α-Fe at room temperature. Γ, Linewidth: 2ε, quadrupole shift; QS, quadrupole splitting; H_{max}, hyperfine field value corresponding to the maximum of the field distribution.

[a] At low temperature, this impurity spectrum cannot be resolved from the whole hyperfine distribution.

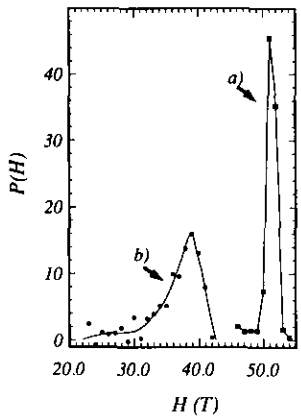

FIG. 10. Fitted hyperfine field distribution $P(H)$ corresponding to the Mössbauer spectra of $YBaCuFeO_5$ at 4.2 K (a) and room temperature (b). The lines are used as a guide for the eyes.

shift $2\varepsilon = -0.06$ mm/sec, and the quadrupole splitting QS = 0.21 mm/s, values observed at 4.2 and 530 K, respectively, lead to $\theta = 68°$ with respect to the relationship

$$2\varepsilon = \mathrm{QS}(3\cos^2\theta - 1)/2$$

in the case of axial symmetry, where θ is the angle defined by the principal axis V_{ZZ} of the electric field gradient tensor and the hyperfine field direction. Such a value agrees well with that proposed by Meyer *et al.* (3).

6. EFG CALCULATIONS

First calculations, restricted to the monopolar contribution of the EFG, were performed on $YBaFeCuO_5$ using a point charge model, in order to give an interpretation of the experimental distribution $P(\mathrm{QS})$ seen in the paramagnetic range (T = 530 K). It is important to note that this numeric approach can only provide qualitative information, because the nonnegligible covalency effects and

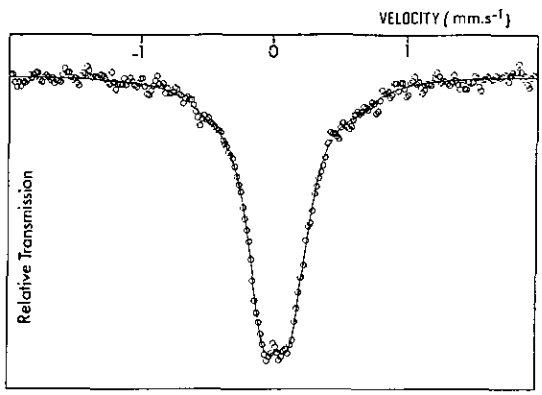

FIG. 11. Mössbauer spectra of $YBaCuFeO_5$ at 530 K.

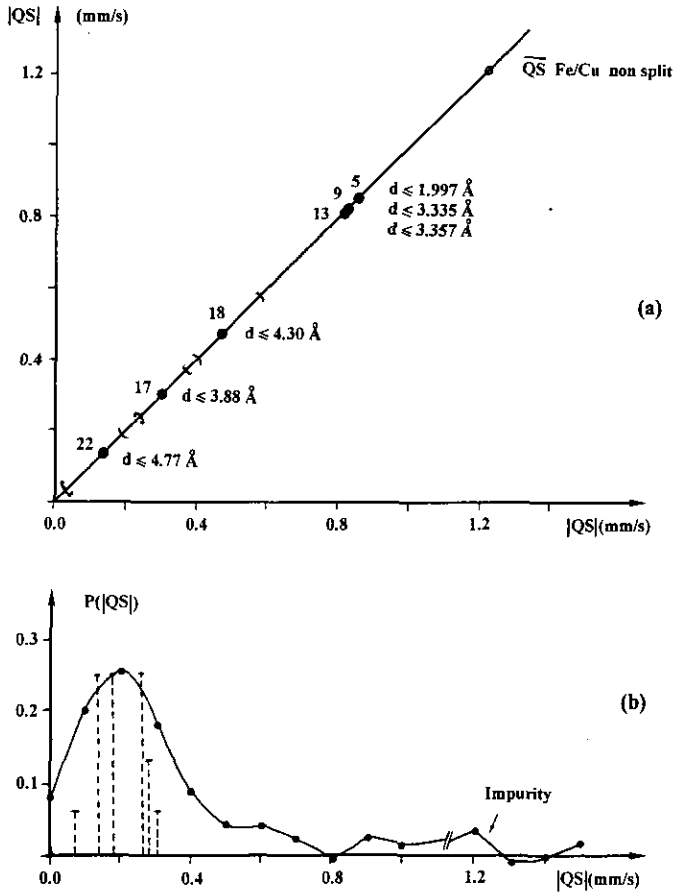

FIG. 12. (a) Evolution of the EFG-calculated |QS| values at 530 K for $YBaCuFeO_5$ as a function of the number of iron next neighbours from 5 to 22 ions, corresponding to d distances in the range 1.997–4.77 Å. For the case of 17, 18, or 22 ions, the effect of a cationic disorder in the Fe–Cu sites must be considered and a dispersion of the |QS| values is observed, noted with parentheses (17), [18], or {22}; the central values of these domains correspond, in each case, to a situation where the Fe and Cu sites are not split. The |QS| = 1.21 mm/sec value corresponds to a fit via the two usual EFG programs applied to the central Fe ion in a mean Fe/Cu position. (b) Mössbauer fitted distribution $P(|\mathrm{QS}|)$ (full circles) and calculated binomial distribution of |QS| for the 22-fold iron environment (dotted lines). The full lines are used as a guide for the eyes.

the temperature dependency cannot be accounted for in the present calculations.

The $3d^5$ electronic shell of iron does not contribute to the iron EFG tensor since only high-spin Fe^{3+} is involved in $YBaFeCuO_5$. So the only contribution to EFG's is the "lattice" one, due to the electrostatic interactions between the iron center and its surrounding ions.

Usually, the monopolar and dipolar contributions to the EFG tensor (lattice term) can be estimated from a summation of polarisable point charges; in the case of a crystalline sample, the monopolar contribution can be calculated either in the reciprocal (9) or in the direct (10)

lattice, whereas the dipolar contribution is self-consistently estimated in the direct lattice. The method consists in lattice summations performed iteratively on volumes resulting from the packing of elementary cells displayed systematically around the origin cell (computing details are given in (10)). Thus, fractional charges must be considered and accurate crystallographic data are required in order to speed up the convergence.

However, in the $YBaCuFeO_5$ structure, iron and copper atoms are randomly distributed in their sites and these sites are split and separated by a distance of about 0.25 Å, as deduced from the Fourier difference synthesis on the neutron results (see above).

The two programs which generate automatically the ionic positions and the charges of the atoms by a translation of the data relative to the central cell are not able to account for randomly distributed situations. An alternative would consist in using a large "supercell" in which the cationic disorder between Fe and Cu sites would be simulated, but this procedure would require high computing times. So these difficulties led us to work only at a monopolar level with the classical programs described above.

As a matter of fact, in this situation, one can only introduce a "mean" position for the Fe and Cu sites of the central cell, to avoid the consequences of artificial simultaneously nonzero occupancies in neighbouring Fe and Cu sites which would generate unrealistic values of the potentials, electric fields, and EFG components.

The results obtained with $z_{Fe-Cu} = 0.2671$ by the two programs working in the reciprocal and direct lattice, respectively, were in agreement and gave an axial V_{ij} tensor ($\eta = 0$) with its principal Z axis along the **c** direction and a positive V_{ZZ} gradient. $QS = (eQ/2) \cdot V_{ZZ}(1 - \gamma_\infty)(1 + \eta^{2/3})^{1/2}$ was found at 1.21 mm/sec, assuming a mean value $Q = 0.2$ barn (11) for the quadrupolar moment of iron in its excited state and an antishielding Sterheimer factor $(1 - \gamma_\infty) = 10.14$ (12) typical for Fe^{3+}. The comparison with the experimental distribution of $|QS|$ values ($0 < |QS| < 1$ mm/sec, with a main peak at about 0.21 mm/sec at 530 K) shows that the above mean value of 1.21 mm/sec is too high. Let us mention that the disagreement subsists, even with lower values of Q encountered in the literature (13). This is the evidence that the mean situation where Fe and Cu are not split is not realistic.

As the above programs cannot account for local situations with atomic displacements, nonstoichiometry, vacancies, or distortions of the environment, we have written a new simpler program (14) (GCEMON) which calculates the EFG lattice tensor of a central iron ion surrounded only by a "cluster" of nearest neighbours defined in the local situation (first, second, . . . types of neighbors can be introduced one by one, as numerous as wanted). Calculations are limited to the monopolar order, owing to the finite limitation in the number of ions and to the numerous unknown polarisability factors involved in the problem. With this program, even if the QS value estimations are rather crude, more realistic comparisons and qualitative interpretations become possible between various neighboring hypothesis. Figure 12a presents the results of successive QS calculations, starting from a fivefold oxygen coordination for iron, adding successively 4 yttrium (iron environment of 9 ions), 4 barium (13 ions), then 4 cations Fe or Cu in the $Fe–O_2$ plane (17 ions), then one apical Cu (18 ions, the situation with an apical Fe has a small probability to be observed and has been neglected here), and at last 4 equatorial O_2 oxygen atoms (22 ions). So our calculation is limited to Fe-ion distances lying in the range (1.997–4.77 Å). In addition to the high sensitivity of the calculated QS values versus the surrounding of the Fe ion, one can note that they become comparable with the experimental data when the integrating sphere radius is larger than 3.4 Å (Fig. 11).

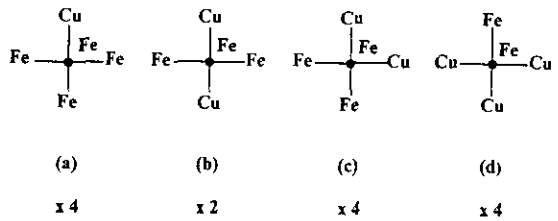

FIG. 13. Some of the 16 in-plane cationic environments of iron, leading to nonaxial EFG tensors (the multiplicity indicates the number of equivalent configurations).

For those of the investigated ion coordinations which respect the axial **c** symmetry of the cluster, the calculated EFG tensors were axial, with a positive V_{ZZ} gradient along **c**, as obtained by the two classical programs in the nonsplit Fe–Cu situation.

The consideration of a cationic disorder in the $Fe–O_2$ plane led also to the investigation of nonaxial situations, such as in Fig. 13, which corresponds either to nonaxial EFG tensors with $\eta = 0.4$, $V_{ZZ} > 0$, and Z in the (**a**, **c**) plane, near **c** (Figs. 13a, 13d), or to nearly axial EFG tensors with Z near to **a** or **b** and $V_{ZZ} < 0$ (Fig. 13b) or near to **c** and $V_{ZZ} > 0$ (Fig. 13c).

In Fig. 14, we have reported the calculated QS values for the maximum iron environment studied ($d < 4.77$ Å), accounting for a binomial distribution of probability in the Fe–Cu sites of the $Fe–O_2$ plane. The results lie in the range $-0.23 < QS < 0.21$ mm/sec. The calculated distribution of $|QS|$ is then reported in Fig. 12b to be compared to the Mössbauer fitted distribution. The agreement is qualitatively correct and, in spite of the crudeness of the present calculations, this numeric approach gives a tendency to account for the $P(QS)$ distribution by the cationic disorder in the $(Fe–Cu)O_2$ planes.

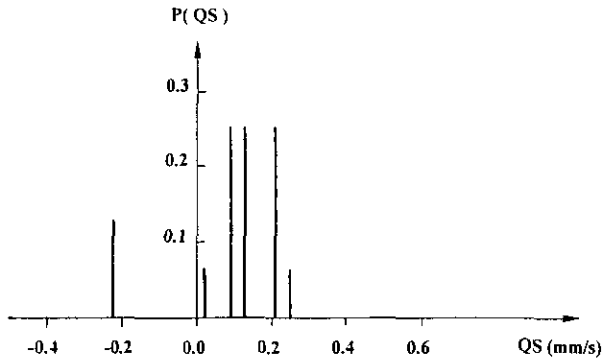

FIG. 14. P(QS) distribution calculated with binomial probabilities in the $(Fe/Cu)O_2$ plane for the 22-fold iron "cluster." (A negative QS value is observed in the case of Fig. 13b, associated with $\eta = 0.2$.)

7. DISCUSSION

The nuclear structure proposed in this work does not question the main conclusion, obtained by C. Meyer *et al.* (3), about the existence of a unique pyramidal oxygen environment for iron in $YBaCuFeO_5$. As expected from chemical consideration, the location of iron inside the oxygen pyramids is different from that of copper, but the geometry of the pyramid is the same for the two cations. Some remarks could be made about trivalent iron in pyramidal coordination:

The apical $Fe–O_1$ distance is shorter than the basal $Fe–O_2$ distance and these interatomic distances agree well with those of structures containing trivalent iron in pyramidal coordination (15–19). Except for the case of $LnTiFeO_5$, the compounds reported in Table 4 are related to the perovskite structure and contain layers of FeO_5 or $(Cu,Fe)O_5$. Bond valence calculation using the Fe^{3+} parameter (20) gave a valence for iron in $YBaCuFeO_5$ close to the calculated value for compounds containing trivalent iron in pyramidal coordination.

The displacement u of iron out of the basal plane of the pyramid toward the apical oxygen, obtained from the nuclear structure refinement, is fairly large, as observed for compounds with iron in pyramidal coordination (Table 4). This value is confirmed by the agreement between the EFG computed and experimental values of the Mössbauer quadrupole splitting for iron. In contrast, the displacement u of copper in related structures is quite short (Table 4). Clearly, as pointed out by Meyer *et al.* (3), during the substitution of iron for copper, iron never occupies the exact Cu position inside the "O_5" pyramid but is displaced with respect to the latter. This shift of iron position, with respect to copper, is of crucial importance for EFG calculations and has been invoked to explain the small quadrupole splitting of iron substituted in the pyramidal copper site for $YBa_2Cu_{3-x}Fe_xO_7$ (21), $Y_{1-x}Ca_xBa_2Cu_{3-x}Fe_xO_7$ (22), and $La_2CaCu_{2-x}Fe_xO_6$ (23).

The hyperfine field at 4 K in $YBaCuFeO_5$ (50.7T (3), 51T (this work)) is comparable to the values observed for trivalent iron in high-spin state ($S = 5/2$) with pyramidal coordination: 52.1T ($Sr_3Fe_2O_6$ (24)), 53.0T ($YBa_2Fe_3O_8$ (25)), and 53.7T ($Pb_4Fe_3O_8Cl$ (26)). A high-spin state for iron is also reported for perovskite-related compounds containing iron and copper ($LnBaCuFeO_5$ (5, 6), $Y_2SrCuFeO_{0.65}$ (18)).

The apical distance $Fe–O_1$ is slightly longer than the most recent neutron structure refinements (on $Sr_3Fe_2O_6$ (15) and $YBa_2Fe_3O_8$ (16)). On the opposite, the apical distance $Cu–O_1$ is in the low range of mean apical distance for divalent pyramidal copper (18, 27–29) (Table 5). The anisotropic thermal parameters of the apical oxygen O_1, with the largest axis of thermal ellipsoid along the **c** axis, suggest that the apical distance $M–O_1$ could be accommodated by small displacements of the apical oxygen; thus a local order may exist where two apex-sharing pyramids are occupied by iron and copper, forming $CuFeO_9$ bipyramidal units.

The results of the structure refinements may appear contradictory with respect to those obtained from Raman

TABLE 4
Relevant Parameters for Trivalent Iron in Pyramidal Coordination

S. G.:	*I4/mmm*	*P4/mmm*	*P4/mmm*	*P4/mmm*	*Ibam*	*Pbam*
Compound:	$Sr_3Fe_2O_6$	$YBa_2Fe_3O_8$	$Pb_4Fe_3O_8Cl$	$YBaCuFeO_5$	$Y_2SrCuFeO_{6.5}$	$LnFeTiO_5$
Ref.:	(15)	(16)	(17)	This work	(18)	(19)
$Fe–O_{basal}$	1.980(1)	2.0138(9)	2.013(7)	2.001(2)	1.989(1)	1.92
					1.995(3)	1.97
					1.996(3)	
					1.956(2)	
$Fe–O_{apical}$	1.886(4)	1.872(6)	1.932(8)	1.927(8)	1.994(1)	1.84
u	0.359	0.467	0.49	0.498	—	0.23
Valence	2.91	2.74	2.64	2.72	2.72	—

and infrared studies by Atanossova *et al.* (30). Considering the number of Raman active modes of $YBaCuFeO_5$ the latter authors concluded that the structure can be described in the acentric group *P4mm* rather than in the centrosymmetric group *P4/mmm*. The neutron diffraction results established that the 2 h site is split into two sites half occupied by iron and copper. Consequently, the local structure is noncentrosymmetric, although the mean structure, based on ND results, is quiet and is described in the centrosymmetric space group. In fact, the neutron diffraction, the Raman, and the infrared data are not incompatible. The main difference between the noncentrosymmetric (1, 3, 30) and the centrosymmetric models is due to the distribution of iron (and copper) in the double pyramidal layer. In the first case (*P4mm* model), one pyramidal $[Fe_2O_5]_\infty$ layer alternated with one $[Cu_2O_5]_\infty$ layer so that in each bilayer each iron atom had the same cationic environment, i.e., was surrounded by four iron and one copper. In our *P4/mmm* model, copper and iron atoms are randomly distributed, forming a $[CuFeO_5]_\infty$ layer so that each iron has a mean number of two iron next neighbors in each single layer. A complete statistical distribution of the transition element species would lead to a mean number of 2.5 iron next neighbors per iron in each double pyramidal layer. Considering the possibility of a local ordering of iron and copper to form $CuFeO_9$ units, the double pyramidal layers consist then of such units arranged in a statistical way, so that the mean number of iron neighbors is reduced to two per iron atom in each bilayer. The random distribution of magnetic atoms with different single-ion magnetic anisotropy might lead to a slight misalignment of the spin directions in the magnetic structure. Moreover, the magnitude and the location of the spin components are also distributed and so are not correlated from site to site. Therefore, the disordered components have no contribution to the Bragg diffraction peaks and their magnetic scattering is distributed in the background of the diffraction pattern leading to a reduction in the refined value of the magnetic moment. This interpretation is fully consistent with the absence of a drastic reduction in the saturated value of the hyperfine field observed by Mössbauer spectroscopy, which records the local field acting at the iron nucleus, whereas only the average ordered components of the spins are observed in the diffraction experiment. The random distribution of iron and copper cations, in a double pyramidal layer, is also observed in the compound $Y_2SrCuFeO_{6.5}$ (18). Mössbauer spectroscopy gives evidence for similar magnetic behaviors of $YBaCuFeO_5$ and $Y_2SrCuFeO_{6.5}$: for these two compounds, there is a progressive and asymmetric broadening of the magnetic sextet lines as the temperature increases and a coexistence of paramagnetic and magnetic contributions near T_N. Moreover, for these compounds, the easy axis of magnetisation is tilted with respect to the **c** axes (about 45° for $Y_2SrCuFeO_{6.5}$ (18)). It is plausible to attribute these observations to the fluctuation of exchange interactions between magnetic atoms in the $(Fe,Cu)O_5$ layers which perturbs the local and long-range magnetic order. The incommensurate magnetic transition, observed below 200 K in $YBaCuFeO_5$, could probably minimise locally the distribution of hyperfine fields acting on magnetic atoms by a rearrangement of the moments. This point could be clarified by performing some high-field Mössbauer spectroscopy experiments. The nature of this short-range ordering is still unknown, due to the small number of magnetic peaks revealed in the neutron powder diffraction experiment.

8. CONCLUSION

This study shows that the $YBaCuFeO_5$ structure can be described in the space group *P4/mmm*; consequently there is only one crystallographic site for copper and iron, respectively, in the tetragonal structure. However, it is important to note that iron is not located at the same position as copper inside the "O_5" pyramid, as shown

TABLE 5
Relevant Parameters for Divalent Copper in Pyramidal Coordination

S. G.:	*I4/mmm*	*I4/mmm*	*P4/mmm*	*P4/mmm*	*Ibam*
Compound:	$La_2SrCu_2O_6$	$La_{1.9}Ca_{1.1}Cu_2O_6$	$YBa_2Cu_3O_6$	$YBaCuFeO_5$	$Y_2SrCuFeO_{6.5}$
Ref.:	(27)	(28)	(29)	This work	(18)
$Cu-O_{basal}$	1.938(1)	1.913(1)	1.939(2)	1.949(1)	1.989(1) 1.995(3) 1.996(3) 1.956(2)
$Cu-O_{apical}$	2.209(4)	2.306(4)	2.470(3)	2.213(11)	1.994(1)
u	0.148	0.057	0.205	0.206	—

from the nuclear structure and as confirmed from Mössbauer spectra and by EFG calculations. From this study, it appears that one must consider the bipyramidal units $CuFeO_9$; i.e., when the O_5 pyramid is occupied by copper, the adjacent one along **c** is occupied by iron. These $CuFeO_9$ units are distributed at random in the $[CuFeO_5]_\infty$ layers. The study of the magnetic behavior of this phase shows its great complexity. For the commensurate magnetic structure, whose moments are characterized by a component in the (**a**, **b**) plane and a possible contribution along **c**, it is not possible to conclude between two kinds of spin ordering along **c**, i.e., +[+−]− or +[−−]+. Besides the latter, the incommensurate phase, with a finite antiferromagnetic spin correlation, is so far not completely studied.

Note added in proof. After the submission of this paper, we received a preprint by Mombru *et al.* (31) which describes the magnetic structure at room temperature and above in the ordered model (*P4mm*). The authors report a stacking sequence +[0−]0 for the iron moment with a small or no copper moment. In spite of this difference, Mombru *et al.* obtained the same values as ours for the iron moment, the Néel temperature, and the critical exponent β. The observed reduction of moment remains unclear in this ordered model.

REFERENCES

1. L. Er-Rakho, C. Michel, Ph. Lacorre, and B. Raveau, *J. Solid State Chem.* **73,** 531 (1988).
2. J. T. Vaughey and K. R. Poeppelmeier, *in* "Proceedings of the International Electronic Ceramics Conference," Special Publication 804, p. 419. National Institute of Standards and Technology, (Washington, DC, 1991.
3. C. Meyer, F. Hartmann-Boutron, Y. Gros, and P. Strobel, *Solid State Commun.* **76,** 163 (1990).
4. M. Pissas, C. Mitros, G. Kallias, V. Psycharis, D. Niarchos, A. Simopoulos, A. Kostikas, C. Christides, and K. Prassides, *Physica C* **185–189,** 553 (1991).
5. M. Pissas, V. Psycharis, C. Mitros, G. Kallias, D. Niarchos, A. Simopoulos, and A. Kostikas, *J. Magn. Magn. Mater.* **104–107,** 571 (1992).
6. M. Pissas, C. Mitros, G. Kallias, V. Psycharis, A. Simopoulos, A. Kostikas, and D. Niarchos, *Physica C* **192,** 35 (1992).
7. J. Rodriguez-Carvajal, *in* "Satellite Meeting on Powder Diffraction," Abstracts of the XVth Conference of the International Union of Crystallography, p. 127. Toulouse, 1990.
8. G. Shirane, *Acta Crystallogr.* **12,** 282 (1959).
9. J. Pannetier, monopolar "LATSUM" program (1978) using Bertaut's series completed by Y. Calage (1983), unpublished.
10. Y. Calage, J. Teillet, and F. Varret, "EFGDIR" program for mono and dipolar lattice EFG tensors (1982), unpublished.
11. P. Gütlich, R. Link, and A. Trautwein, *in* "Mössbauer Spectroscopy and Transition Metal Chemistry." Springer-Verlag, Berlin, 1978.
12. R. M. Sternheimer, *Phys. Rev.* **130,** 1423 (1963).
13. K. J. Duff, K. C. Mishra, and T. P. Das, *Phys. Rev. Lett.* **46,** 1611 (1981).
14. A. Ducouret-Cérèze, monopolar "GCEMON" program (1992), unpublished.
15. S. Dann, M. T. Weller, and D. B. Currie, *J. Solid State Chem.* **97,** 179 (1992).
16. Q. Huang, P. Karen, V. L. Karen, A. Kjekshus, J. W. Lynn, N. Rosov, and A. Santoro, *Phys. Rev. B* **45,** 9611 (1992).
17. J. Pannetier and P. Batail, *J. Solid State Chem.* **39,** 15 (1981).
18. J. S. Kim, J. Y. Lee, J. S. Swinnea, H. Steinfink, W. M. Reiff, P. Lightfoot, S. Pei, and J. D. Jorgensen, *J. Solid State Chem.* **90,** 331 (1991).
19. G. Buisson, *J. Phys. Chem. Solids* **31,** 1171 (1970).
20. I. D. Brown and D. Altermatt, *Acta Crystallog. B* **41,** 244 (1985).
21. F. Hartmann-Boutron, C. Meyer, Y. Gros, and P. Strobel, *Hyperfine Interact.* **55,** 1229 (1990).
22. A. Rykov, A. Ducouret, N. Nguyen, V. Caignaert, F. Studer, and B. Raveau, *Hyperfine Interact.* **77,** 277 (1993).
23. C. Meyer, F. Hartmann-Boutron, Y. Gros, and P. Strobel, *Physica C* **181,** 1 (1991).
24. P. K. Gallagher, J. B. MacChesney, and D. N. E. Buchanan, *J. Chem. Phys.* **45,** 2466 (1966).
25. I. Felner, I. Novik, U. Yaron, O. Cohen, E. R. Bauminger, T. Kroener, and G. Czjzek, *Phys. Rev. B* **48,** 16040 (1993).
26. J. Emery, A. Cerese, and F. Varret, *J. Phys. Chem. Solids* **41,** 1035 (1980).
27. V. Caignaert, N. Nguyen, and B. Raveau, *Mater. Res. Bull.* **25,** 199, (1990).
28. F. Izumi, E. Takayama-Muromachi, Y. Nakay, and H. Asano, *Physica C* **157,** 89 (1989).
29. G. Roth, B. Renker, G. Heger, M. Hervieu, B. Domenges, and B. Raveau, *Z. Phys. B* **69,** 53 (1987).
30. Y. K. Atanassova, V. N. Popov, G. G. Bogachev, M. N. Iliev, C. Mitros, V. Psycharis, and M. Pissas, *Phys. Rev. B* **47,** 15201 (1993).
31. A. W. Mombru, C. Christides, A. Lappas, K. Prassides, M. Pissas, C. Mitros, and D. Niarchos, *Inorg. Chem.*, **33,** 1255 (1994).